Research Square

Preprints are preliminary reports that have not undergone peer review.
They should not be considered conclusive, used to inform clinical practice,
or referenced by the media as validated information.

Experimental and numerical investigation of cold forging tool degradation due to plastic deformation

Erikson Athos Portugal Pressi
Military Institute of Engineering
Carlos Maurício Sacchelli
Universidade Federal de Santa Catarina
Sérgio Junichi Idehara
sergio.idehara@ufsc.br

Universidade Federal de Santa Catarina
Marcos Alves Rabelo
Universidade Federal de Santa Catarina

Research Article

Keywords: Cold forging, H13 steel, Johnson Cook model, finite element method

Posted Date: August 13th, 2026

DOI: https://doi.org/10.21203/rs.3.rs-10627281/v1

License: This work is licensed under a Creative Commons Attribution 4.0 International License.
Read Full License

Additional Declarations: No competing interests reported.

TITLE PAGE

Title
Experimental and numerical investigation of cold forging tool degradation due to plastic deformation

Author information
Erikson Athos Portugal Pressi, erikson.athos@ime.eb.br[1]
Carlos Maurício Sacchelli, carlos.sacchelli@ufsc.br[2]
Sérgio Junichi Idehara, sergio.idehara@ufsc.br[3]
Marcos Alves Rabelo, marcos.rabelo@ufsc.br[2]

[1]Military Institute of Engineering, Rio de Janeiro, RJ, Brazil
[2]Federal University of Santa Catarina, Joinville, Santa Catarina, Brazil
[3]Federal University of Santa Catarina, Joinville, Santa Catarina, Brazil, ORCID 0000-0002-3853-0758, corresponding author

Abstract
Cold forging tools are subjected to repeated high contact pressures that may cause progressive plastic strain accumulation, residual stress development, and premature failure. This study presents an experimental–numerical methodology to evaluate plastic deformation and lifetime prediction in an AISI H13 cold forging tool. A cylindrical H13 tool was tested in a hydraulic press under repeated loading against a W350 steel die. The tool response was measured using a strain-gauge rosette and a load cell, allowing the effective strain, stress state, residual strain, and damage evolution to be estimated during the press cycles. The experimental data was used to adjust an analytical Johnson-Cook based plastic strain model and to validate a finite element model developed in QForm software. The results showed that tool fracture occurred when the accumulated permanent effective strain reached 6,674 μstrain. The adjusted Johnson-Cook model predicted failure close to the experimental fracture strain and before the phase of imminent material failure, whereas the FEM-based damage model predicted failure after a higher number of cycles, but before the tool fracture. The FEM model also reproduced the local plastic strain at the strain-gauge position with a difference of 4.37% relative to the experimental measurement. These results indicate that integrating strain measurements with analytical modeling and FEM simulation can support tool degradation assessment and lifetime prediction under low-cycle fatigue conditions.

Keywords
Cold forging; H13 steel; Johnson Cook model; finite element method

Acknowledgment
The authors thank SixPro for their assistance with the QForm simulations. This study was financially supported by the Research Development Foundation (Fundação de Desenvolvimento da Pesquisa – Fundep), through the Rota 2030 Program, Line IV, grant number 27194*37.

1. Introduction

Cold forging is widely used for manufacturing metallic components with high productivity and repeatability, as well as good dimensional accuracy, surface quality, and material savings (Pilc et al. 2014). However, the stability of the process depends strongly on the mechanical integrity of the forming tools, since tool degradation and failure may affect material flow, final component geometry, forming load, and production costs. In cold forging, tool service life is directly related to process productivity and product quality, and initial tool damage is commonly associated with plastic deformation, abrasive wear, and fatigue of the working surfaces (Dalbosco et al. 2021). Backward extrusion is particularly demanding because large forming forces and frictional stresses act on the punch and die, making die performance a limiting factor for process viability and production cost (Petkar et al. 2026). Forging tools are subjected to repeated high contact pressures and cyclic loading, which may lead to wear, fatigue cracking, thermal softening, and localized plastic deformation (Varničić et al. 2023). It has been estimated that 70% of tools are withdrawn from service due to plastic deformation or abrasive wear (Ficak et al. 2024). Plastic deformation of the tool is especially relevant because even small permanent changes in die geometry may alter the forged part dimensions and the stress state during subsequent cycles.

AISI H13 tool steel is commonly used in forging dies due to its combination of relatively hardness, toughness, fatigue resistance, and resistance to thermal cracking (Marashi et al., 2017; Li et al., 2025). Nevertheless, under severe contact conditions, localized stresses may exceed the yield strength of the tool material, leading to progressive plastic strain accumulation, loss of the original tool profile, or tool failure. Experimental studies on H13 steel have shown that carbides and non-metallic inclusions influence crack initiation and propagation during plastic deformation, especially when large particles promote dislocation pileups and stress concentrations (Li et al., 2025). Under forging conditions, Marashi et al. (2017) showed that localized stresses and strains in H13 tools can produce severe deformation accompanied by microstructural changes, including recrystallized regions, martensitic regions, and transition zones. Similar die-life studies have shown that plastic deformation should be evaluated by comparing the effective stress state with the yield strength, hardness, or degradation condition of the tool material (Kim et al. 2005). In hot and warm forging, thermal softening may reduce die hardness and accelerate failure by plastic deformation (Ahmed et al. 2022; Vianello et al. 2020). Although the thermal contribution is less severe in cold forging, cyclic contact pressures, high normal stresses, and friction remain limiting factors for tool degradation (Petkar et al. 2026).

Numerical simulation has become an important tool for designing forging processes (Varničić et al. 2023). With the development of metal forming software, such as Eesy-2-form (Dalbosco et al. 2021), Simufact Forming (Ahmed et al. 2022), and QForm (Vianello et al. 2020), finite element models have been used to determine stress distributions in tools and to predict critical regions for wear and fatigue. These virtual models can represent the workpiece flow stress, forming energy, friction conditions, and the interaction between the workpiece and the forging tools. However, many industrial simulations still treat the tool as rigid or focus mainly on workpiece deformation. This assumption may be adequate for estimating global forming trends, but it limits the prediction of elastic and plastic deformation in the tool itself. When the tool is considered as a rigid body in forging simulations, the elastic strain of the tool may be overestimated, and the dimensions of the forged part may differ from the experimental results (Lee et al. 2002). For this reason, coupled simulations that include material flow and elastic tool behavior have been used to evaluate tool deflection and its effect on the geometric accuracy of forged components (Rohrmoser et al. 2021).

The current literature still lacks experimentally supported numerical procedures capable of evaluating how the mechanical response of a cold forging tool changes after cyclic degradation. Previous studies have investigated tool life (Lachowicz et al. 2025), contact pressure (Varničić et al. 2023), abrasive and adhesive wear (Hsia and Shih 2015; Behrens et al. 2021), fatigue cracking (Dalbosco et al. 2021), fracture prediction (Lisiecki et al. 2025), thermal fatigue (Ficak et al. 2024), surface coatings (Petkar et al. 2026), tool geometry optimization using finite element

models (Rohrmoser et al. 2021), and industrial monitoring (Seo 2022). However, experimental validation remains essential because numerical models are sensitive to material properties, boundary conditions, friction, and tool–workpiece interactions. This limitation is also recognized in die-life prediction studies, in which FEM-based predictions may not fully represent industrial variables such as die alignment, material size deviations, and working temperature, thereby motivating the use of real-time forming load monitoring (Seo 2022). For example, Hsia and Shih (2015) compared finite element predictions with manufacturing data and observed adhesive wear on the punch surface, while Behrens et al. (2021) combined numerical wear calculations with experimental investigations of worn dies. DIC-supported forging studies have also shown that experimental strain fields can be used to validate numerical simulations and identify deformation concentration regions related to fracture initiation (Lisiecki et al. 2025). In this context, there is still limited discussion on how the stress–strain response of H13 steel in raw and degraded conditions can be incorporated into process simulations to assess the onset and evolution of tool plastic deformation up to failure.

In forging processes, tool degradation refers to the progressive deterioration of the mechanical, geometrical, and functional condition of the tool during repeated forming cycles. This deterioration may result from interacting mechanisms, including abrasive and adhesive wear, plastic deformation, mechanical and thermomechanical fatigue, and oxidation. Among these mechanisms, plastic deformation is particularly relevant when localized stress exceeds the yield strength of the tool material, since the accumulation of permanent strain can progressively alter the tool geometry and mechanical response. In the present study, tool degradation is specifically associated with the progressive accumulation of permanent plastic strain in the H13 tool. In this context, there is still limited discussion on how the stress–strain response of H13 steel in its initial and degraded conditions can be incorporated into process simulations to assess the onset and evolution of tool plastic deformation up to failure.

Therefore, this study aims to investigate cold forging tool degradation caused by plastic strain using an integrated experimental-numerical methodology. The work combines strain measurements obtained during forging tests on AISI H13 tool steel in raw and degraded conditions with finite element simulations in QForm (Vianello et al. 2020) to evaluate tool material deformation and predict tool lifetime. The novelty of this work is the integration of local strain-gauge measurements with FEM-based spatial strain amplification to estimate damage accumulation at an inaccessible critical region of a cold-forging tool.

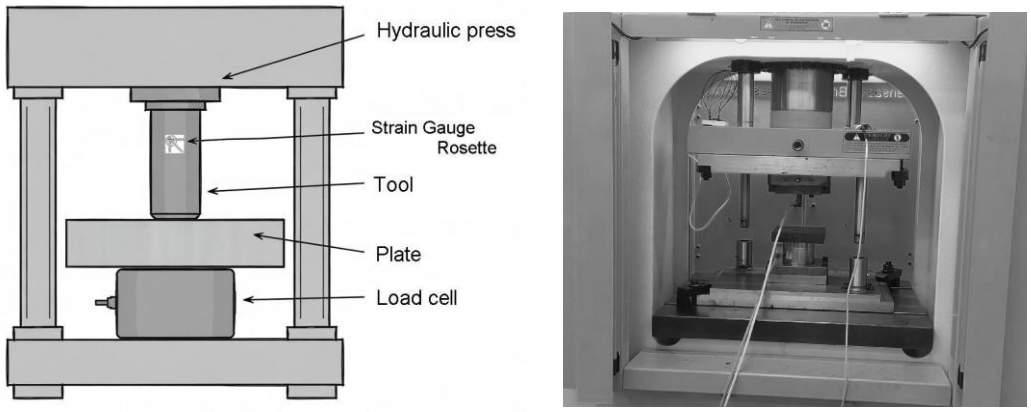
2. Materials and Methods

To characterize forging tool degradation and model tool lifetime, this work developed a simplified experimental configuration in which a cylindrical tool was pressed directly against a flat surface. This geometry enabled the overall stress state to be evaluated under controlled test conditions and correlated with numerical and analytical models. The flat surface, representing the workpiece position, was also manufactured from forging tool steel. The tests were conducted using a conventional hydraulic forging system, and the process was subsequently reproduced numerically using the finite element method.

2.1 Experimental setup

The test was performed using a hydraulic press (**Fig. 1**), commonly employed in the mechanical industry (Pan et al. 2019). A 40-ton press manufactured by Prensas Brasil was used with a 14 mm diameter and 22 mm long H13 steel tool. The chemical composition of the H13 steel is given in **Table 1**. The contact surface of the tool had a mean hardness of 48 HRC. The experiment focused on the behavior of the tool and machine and consisted of repeated press actuations against a W350 steel die. The press reached its maximum operating pressure of 200bar, corresponding to 40tons, over 500 cycles. **Fig. 1a** shows the sensor layout installed on the hydraulic press. For tool instrumentation, a 500kN HBM C6B load cell was used for force measurement. A rectangular strain-gauge rosette (Kyowa, 0°–45°–90°), shown in **Fig. 1b**, was bonded to the tool surface and

used for mechanical strain measurement at 6 mm from the upper flange of the tool. The sensor signals were acquired using a Lynx Tecnologia ADS 2002 data acquisition system at a sampling rate of 10,000Hz, with a 3,000Hz anti-aliasing filter and 16-bit resolution.



(a) (b)

Fig. 1 (a) Schematic layout of the forging tool instrumentation, including the strain-gauge and load cell. (b) Hydraulic press with the experimental setup

Table 1 Chemical composition of the H13 tool steel

Element	Composition range (wt.%)
Chromium, Cr	4.75-5.50
Molybdenum, Mo	1.10-1.75
Silicon, Si	0.80-1.20
Vanadium, V	0.80-1.20
Carbon, C	0.32-0.45
Nickel, Ni	0.30 max.
Copper, Cu	0.25 max.
Manganese, Mn	0.20-0.50
Phosphorus, P	0.03 max.
Sulfur, S	0.03 max.

2.2 Experimental data processing for effective strain

Since this study uses strain-gauge rosette measurements to quantify a local multiaxial strain state, the measured strain field was converted into principal strains and equivalent strain based on solid mechanics formulations. The strain-gauge rosette measured strain in three directions: ϵ_0, aligned with the longitudinal direction of the tool; ϵ_{90}, aligned with the circumferential direction; and ϵ_{45}, oriented at 45° between the longitudinal and circumferential axes.

From the strain measurements in these three directions, the engineering shear strain γ_{xy} was calculated as:

$$\gamma_{xy} = 2\epsilon_{45} - \epsilon_0 - \epsilon_{90} \tag{1}$$

The principal strains at the strain-gauge location, $\epsilon_{1,2}$, were then obtained as:

$$\epsilon_{1,2} = \frac{\epsilon_0 + \epsilon_{90}}{2} \pm \sqrt{\left(\frac{\epsilon_0 - \epsilon_{90}}{2}\right)^2 + \left(\frac{\gamma_{xy}}{2}\right)^2} \tag{2}$$

Assuming a plane stress state on the tool surface, the stress components were calculated as σ_x in the longitudinal direction, σ_y in the circumferential direction, and τ_{xy} as the shear stress. In these equations, E is Young's modulus, ν is Poisson's ratio, and G is the shear modulus:

$$\sigma_x = \frac{E}{1-\nu^2}(\epsilon_0 + \nu\,\epsilon_{90}) \tag{3}$$

$$\sigma_y = \frac{E}{1-\nu^2}(\epsilon_{90} + \nu\,\epsilon_0) \tag{4}$$

$$\tau_{xy} = G\,\gamma_{xy} \tag{5}$$

The values used in the calculations were $E = 210GPa$ and $\nu = 0.3$. From the calculated stress components, the principal stresses, σ_1 and σ_2, were determined as:

$$\sigma_{1,2} = \frac{\sigma_x + \sigma_y}{2} \pm \sqrt{\left(\frac{\sigma_x - \sigma_y}{2}\right)^2 + \tau_{xy}^2} \tag{6}$$

The equivalent von Mises stress, σ_{vm}, was calculated as:

$$\sigma_{vm} = \sqrt{\sigma_x^2 - \sigma_x\,\sigma_y + \sigma_y^2 + 3\,\tau_{xy}^2} \tag{7}$$

Similarly, the effective strain, also referred to as the equivalent strain, was calculated based on the von Mises criterion, as given in Eq. (8). Under the plane stress assumption adopted for the tool surface, the out-of-plane strain ε_3 was estimated from Poisson's effect.

$$\epsilon_{eff} = \frac{\sqrt{2}}{3}\sqrt{(\epsilon_1 - \epsilon_2)^2 + (\epsilon_2 - \epsilon_3)^2 + (\epsilon_3 - \epsilon_1)^2} \tag{8}$$

The experimental data obtained from the strain-gauge rosette was processed according to the previous equations to determine the effective strain during press actuation. The residual effective strain measured after the press cycles was interpreted as the permanent plastic deformation accumulated during tool operation.

Based on the calculated stress state, the normal stress (σ_n) on a plane inclined at an angle (θ) was determined as:

$$\sigma_n = \frac{\sigma_x}{2}\,(1 + cos2\theta) + \frac{\sigma_y}{2}(1 - cos2\theta) + \tau_{xy}\,sin2\theta \tag{9}$$

Similarly, the shear stress (τ) on the plane inclined at an angle (θ) was determined as:

$$\tau = \frac{\sigma_x - \sigma_y}{2}\,sin2\theta - \tau_{xy}\,cos2\theta \tag{10}$$

where $\theta = 0$ represents the original measurement orientation at the strain-gauge location.

The corresponding Mohr's circle was defined by its radius, R, and center coordinate, C.

$$R = \frac{1}{2}\sqrt{\left(\sigma_x - \sigma_y\right)^2 + 4\,\tau_{xy}^2} \tag{11}$$

$$C = \left(\frac{\sigma_x + \sigma_y}{2}, 0\right) \tag{12}$$

2.3 Johnson-Cook Model for Plastic Strain

For ductile materials subjected to high strain rates, the Johnson-Cook model relates the von Mises flow stress (σ_{JC}) to the plastic strain and plastic strain rate. This formulation has been used for material failure characterization, as described by Dabboussi and Nemes (2005), and is given in Eq. (13). The model variables ϵ_p and $\dot{\epsilon}_p$ represent the equivalent plastic strain and the plastic strain rate, respectively, while $\dot{\epsilon}_o$ is the reference strain rate.

$$\sigma_{JC} = \left(A + B\,\epsilon_p^n\right)\left[1 + C\;ln\;ln\left(\frac{\dot{\epsilon}_p}{\dot{\epsilon}_o}\right)\right](1 - T^{*m}) \tag{13}$$

where A is the initial yield strength, B and n describe the strain-hardening behavior, C is the strain-rate sensitivity coefficient, and m is a material constant adjusted in this work.

The first term in parentheses represents strain hardening, the second term accounts for strain-rate sensitivity, and the last term describes thermal softening as a function of the instantaneous working temperature, T_{inst}. In this formulation, T_o and T_{melt} are the reference temperature, usually taken as room temperature, and the material melting temperature, respectively. The homologous temperature ratio is defined as:

$$T^* = \frac{T_{inst} - T_o}{T_{melt} - T_o} \tag{14}$$

The equivalent plastic strain can then be expressed as a function of stress as:

$$\epsilon_p = \left\{\frac{\sigma_{JC}}{\left[1 + C\;ln\;ln\left(\frac{\dot{\epsilon}_p}{\dot{\epsilon}_o}\right)\right](1 - T^{*m})\,B} - \frac{A}{B}\right\}^{1/n} \tag{15}$$

Because the experimental tests were performed at ambient temperature, the homologous temperature was assumed to be $T^* = 0$. With this simplification, the Johnson-Cook model reduces to a Ludwik-type hardening equation (Wuertemberger and Palazotto, 2016). The yield stress was estimated from the load-cell force, F, and the contact area associated with the tool diameter, D. This force-based stress estimate was used to calculate plastic strain. Thus, the Johnson-Cook plastic strain for one press cycle, when the n-th root exists, is:

$$\epsilon_p = \{\left(\frac{4\,F}{\pi\,D^2\,B} - \frac{A}{B}\right)^{1/n}, \quad for\ \left(\frac{4\,F}{\pi\,D^2\,B} - \frac{A}{B}\right) \in R^+\ \ 0, \quad otherwise \tag{16}$$

The constants in Eq. (16) were updated using a nonlinear least-squares method. The objective function minimized the error between the accumulated strain obtained from the experimental data and the predicted accumulated plastic strain, $\sum\epsilon_p$. The fitting procedure was performed over different stress and plastic strain levels, as follows:

$$\left\|\epsilon_p(A,B,F) - \epsilon_p^{exp}(\sigma_{vm})\right\|^2 = \sum_i \left(\epsilon_p(A,B,F_i) - \epsilon_{p_i}^{exp}\left(\sigma_{vm_i}\right)\right)^2 \tag{17}$$

For failure prediction, tool damage was assumed to accumulate as a function of the plastic strain generated in each cycle. Failure was considered to occur when the accumulated damage reached a critical limit defined by the fracture strain, ϵ_{fail}. Therefore, the damage accumulation, D, is expressed as:

$$D = \frac{\sum\epsilon_p}{\epsilon_{fail}} \tag{18}$$

Material failure is assumed to occur when $D \geq 1$ at the location of maximum effective strain. In the experimental evaluation, the onset of structural failure was identified when the plastic strain curve, plotted as a function of time, diverged from the expected continuous trend and visible bending of the tool was observed. The damage parameter was used as an engineering indicator of accumulated plastic deformation rather than as a complete fatigue-life law. Its purpose was to identify the transition to a critical degradation region using measurable strain data.

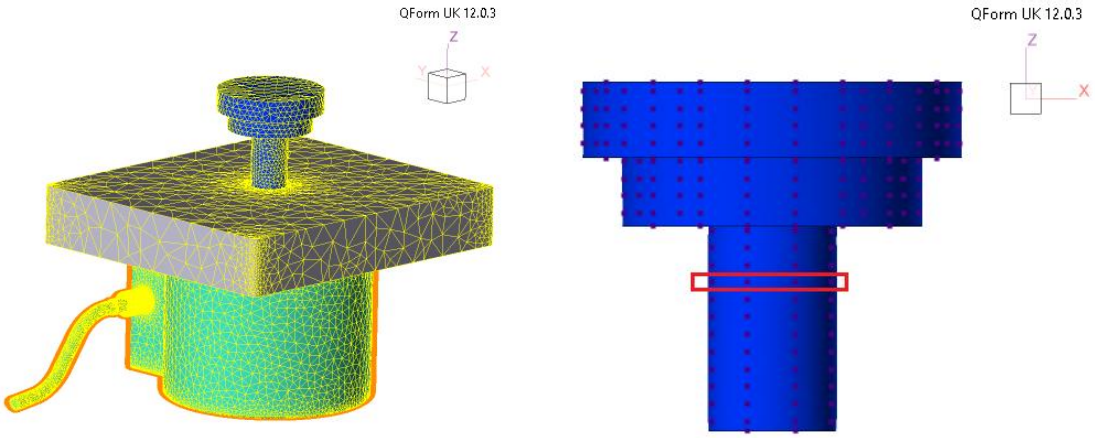
2.4 Numerical Model Based on the Finite Element Method

The experimental test setup was represented using a three-dimensional Finite Element Model (FEM) in QForm, as shown in **Fig. 2**. In this model, Tool 1, located at the top, was defined as the moving component and displaced the specimen in the (+z) direction, while Tool 2, located at the bottom, remained stationary and represented the load cell. As a boundary condition, the velocity of Tool 1 was set to 0.5mm/s, corresponding to the deformation velocity obtained from the experimental data. The material assigned to the simulated tool was AISI H13 steel, with a density of 7,716 kg/m³, Young's modulus of 210 GPa, Poisson's ratio of 0.30, and yield stress of 1,607 MPa. The specimen was modeled using the properties of W350 steel, with a density of 7,800 kg/m³, Young's modulus of 214.3 GPa, Poisson's ratio of 0.30, and yield stress of 1,575 MPa. In the FEM model shown in **Fig. 2a**, the workpiece, Tool 1, and Tool 2 contained 14,401, 1,638, and 70,931 nodes, respectively, and 68,047, 6,337, and 291,086 elements, respectively.

The software uses a bilinear elastic–plastic model with a hardening coefficient, k, which defines the variation in material strength during plastic deformation. The relationship between stress increment, $\Delta\sigma$, and the strain increment, $\Delta\epsilon$, in the material flow rule is expressed as:

$$\Delta\sigma = \{\frac{3E}{2(1+\nu)}\ \Delta\epsilon, \qquad for\ elastic\ phase\ k\ E\ \Delta\epsilon, \qquad for\ plastic\ phase \tag{19}$$

The hardening coefficient was adjusted based on the experimental data from the press actuation at $t = 32s$, resulting in $k = 0.018$. For this adjustment, the initial tool condition was used to compare the elastic and plastic deformation responses obtained from the FEM model and the experimental data. This approach was adopted because material degradation after a long sequence of press actuations affects the stress–strain curve. The actuation force used as the input vector for the simulation is shown in **Fig. 3**. Based on the time-dependent force input, the model provided the strain and stress distributions along the tool geometry, which varied according to the force amplitude. Permanent strain was evaluated after the peak force, when the tool returned to the unloaded condition, whereas the maximum stress was identified at the instant of peak force.



(a) (b)

Fig. 2 Finite element model from QForm. (a) Mesh setup with tool, plate and load cell. (b) Tool with tracking points. Highlighted the region of strain-gauge position

To compare the FEM model with the experimental strain-gauge measurements, tracking points were defined on Tool 1, as illustrated in **Fig. 2b**. The highlighted area indicates the strain-gauge installation region, where eight tracking points were positioned around the circumference of the cylindrical tool.

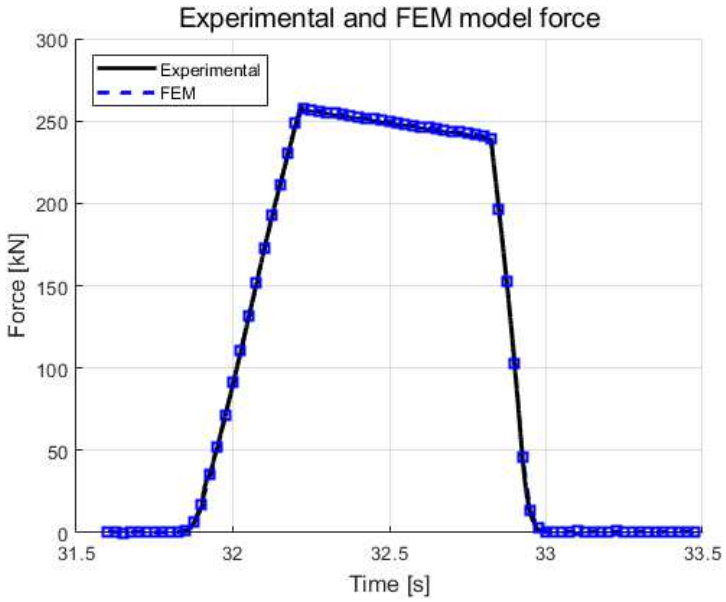


Fig. 3 Force input applied to the FEM model

3. Results

The following results compare the experimental data with the analytical Johnson-Cook model and the FEM model developed in QForm, as described in the previous section. These models can be used to estimate tool lifetime in highly demanding applications, where plastic strain accumulation and low-cycle fatigue are expected to govern tool degradation.

3.1 Experimental tool behavior based on material strain

The experimental test was evaluated with 672 cycles, corresponding to 1,277s. As shown in **Fig. 4**, the effective strain calculated using Eq. (8) varied with the number of cycles, following the variation in press force. During the first 660s, the maximum force ranged from approximately 45kN to 265kN. This force variation was associated with the stabilization of the hydraulic press during the machine setup. After 700s, the press actuation pressure stabilized, maintaining a force of approximately 300kN. Under these conditions, the effective strain showed lower permanent strain accumulation during the first part of the test, when the force remained below 265kN. In this stage, the strain was predominantly in the elastic regime, reaching approximately 4,300µstrain at the force peak. In the second part of the test, when the force reached approximately 300kN, the plastic strain increased monotonically. At approximately 805s, the elastic strain, which had previously been greater than the permanent strain, became lower than the permanent strain during press actuation. Structural failure occurred in the 1,260s, as indicated by the sharp increase in the slope of the permanent strain curve, which reached approximately 6,674µstrain. The final tool condition is shown in **Fig. 5**. The cylindrical tool bent laterally and cracked near the support flange.

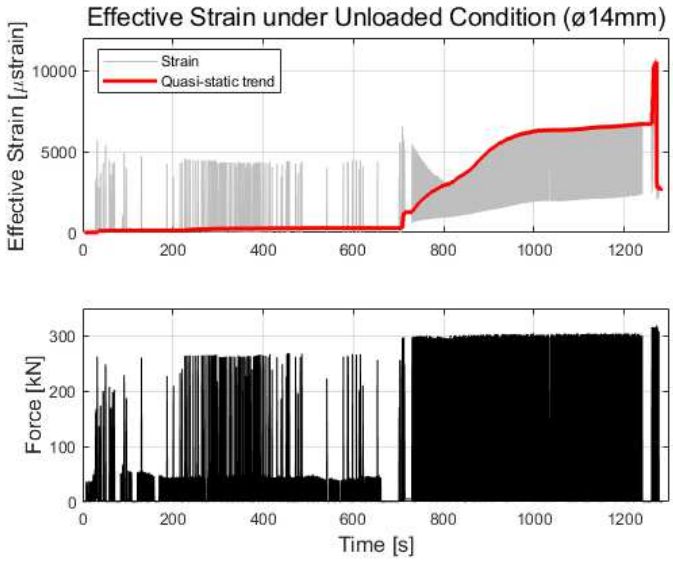
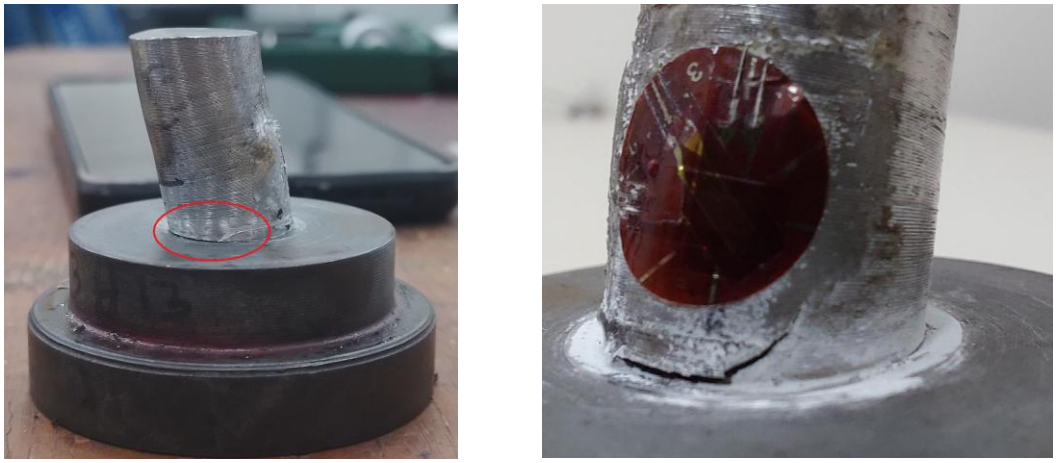


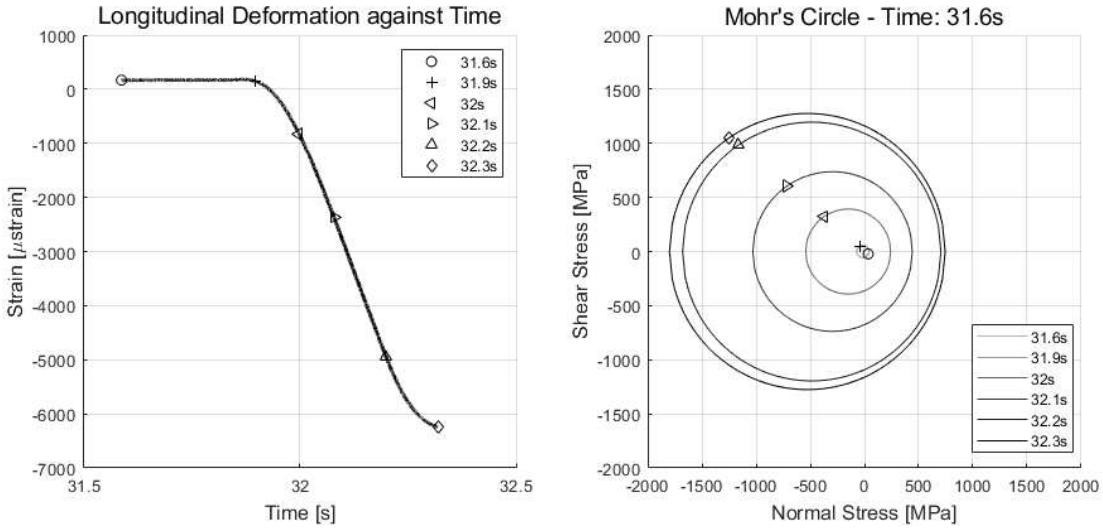
Fig. 4 Effective strain response of the H13 tool during hydraulic press cycles. The highlighted curve indicates the plastic strain measured under the unloaded condition



(a) (b)

Fig. 5 (a) H13 tool after testing until failure, highlighting the material crack region. (b) Enlarged view of the crack region and strain-gauge

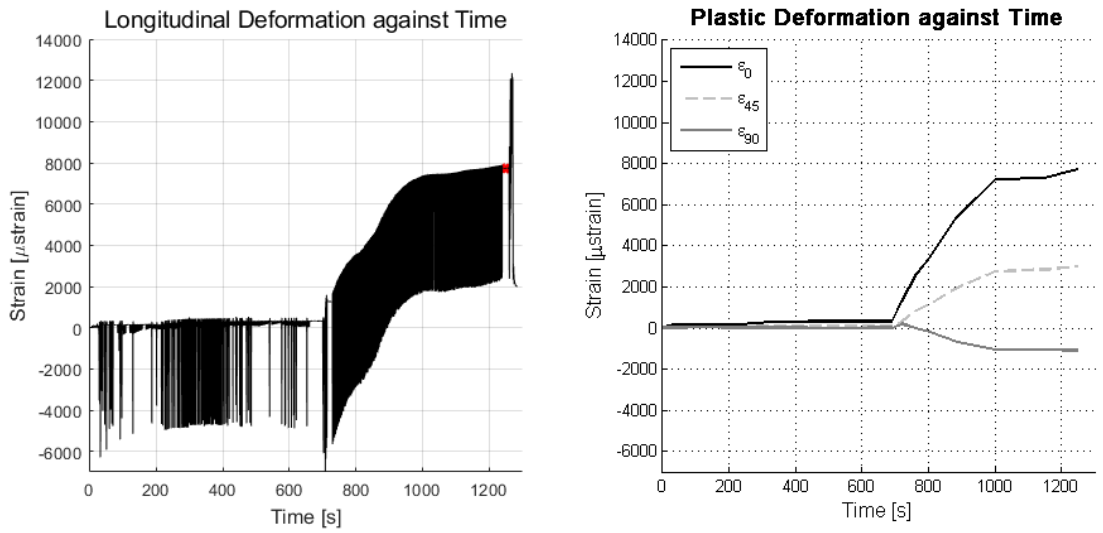
To verify the correlation between the strain measured by the strain-gauge and the stress estimated from the load cell, one cycle at $t = 32s$ was analyzed. This cycle occurred in the elastic region and reached a peak force of 262.4kN, corresponding to an average compressive stress of $\sigma = 1{,}704.60MPa$. Under this condition, the maximum longitudinal compressive strain was 6,237μstrain, as shown by the continuous curve in **Fig. 6a**. Based on the rosette strain measurements, the maximum compressive normal stress calculated using Eq. (9) was 1,794MPa, as represented by Mohr's circle in **Fig. 6b**. The difference between the load-cell-based stress estimate and the strain-gauge-based stress estimate was less than 5.3%, considering the adopted material properties. Since this difference was relatively small, these values were used as material parameters in the subsequent models.



(a) (b)

Fig. 6 (a) Strain response during one press actuation cycle. (b) Mohr's circle of stress states during material compression

Subsequently, the complete longitudinal strain response is shown in **Fig. 7a**. In the first part of the test, before 700 s, the longitudinal plastic strain remained relatively low, reaching 319μstrain. After this point, due to the higher press force, the plastic strain increased continuously until fracture, reaching a longitudinal strain of 7,732μstrain. The accumulation of plastic deformation in the structure leads to the development of residual stress. According to Zhu (2023), large plastic deformation combined with cold residual stresses can alter the mechanical behavior of cracks by changing the crack-driving force within the residual stress field. This condition differentiates forging fatigue life from conventional material fatigue failure, in which residual stress levels are generally lower due to the absence of high repetitive impact forces. **Fig. 7b** presents the permanent strain measured by each strain-gauge in the longitudinal (ϵ_0), circumferential (ϵ_{90}), and inclined (ϵ_{45}) directions. Similar to the effective strain curve, the strain increase before 700s was relatively low and increased considerably after the maximum machine force was reached. In the longitudinal and inclined directions, the accumulated strain was positive, indicating tensile deformation, whereas in the circumferential direction, the accumulated strain was negative, indicating compressive deformation.



(a) (b)

Fig. 7 (a) Longitudinal strain response showing plastic strain accumulation. (b) Plastic strain measured by the strain-gauge in the longitudinal (ϵ_0), inclined (ϵ_{45}) and circumferential (ϵ_{90}) directions

3.2 Johnson-Cook model adjustment for plastic strain

Application of the Johnson-Cook model in Eq. (16) to the experimental data using Eq. (17) resulted in the curve shown in **Fig. 8**. The updated model parameters were $A = 1{,}738.59MPa$, $B = 1{,}000.00MPa$, $C = 0$ and $n = 0.15$. These results indicate a low dependence on strain rate for the representation of the forging condition, as shown by the zero-value obtained for the strain-rate coefficient, C. The plastic strain per cycle shown in **Fig. 8** is presented as a function of the nominal peak stress during press actuation. In phase A, the model response showed low amplitude, following the lower level of the experimental data, below 0.2µstrain. In phase B, the model showed a high slope gradient, compatible with the increase in permanent strain observed experimentally. The last phase, phase C, represents material fracture, which cannot be directly identified by this model. The updated model was focused on phase B, where permanent material deformation occurs and leads to tool failure under low-cycle fatigue conditions.

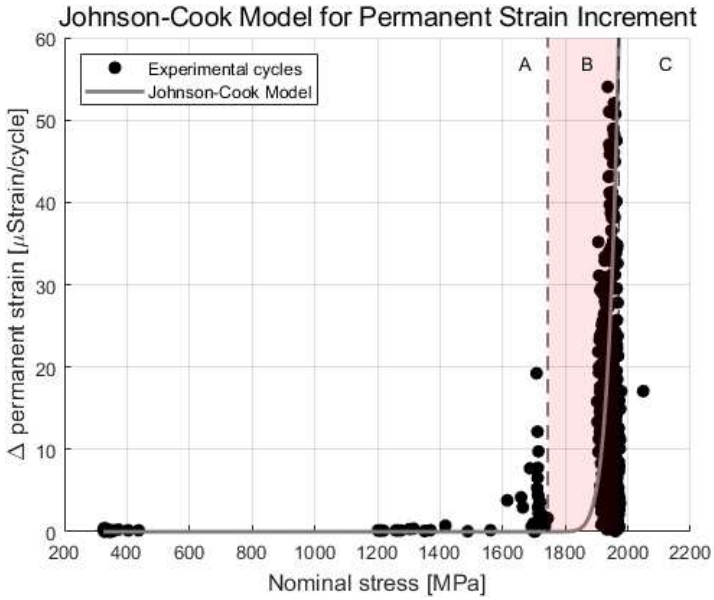


Fig. 8 Plastic strain per cycle in the H13 tool as a function of nominal average stress

Using the adjusted Johnson-Cook model, the experimentally based cycle history was simulated by using the measured peak force of each cycle to calculate stress and estimate the corresponding plastic strain. **Fig. 9** shows the accumulation of permanent strain as a function of the number of cycles. In the experimental test, fracture occurred at cycle 656, corresponding to the last cycle before visible tool bending, when the accumulated permanent effective strain reached 6,674µstrain. Using the model, failure was predicted when the accumulated strain reached the same effective failure strain, which occurred at cycle 439. This corresponds to a predicted lifetime approximately 33% lower than that observed experimentally. In phase B, the experimental strain accumulation rate was approximately 19.9µstrain/cycle, based on a linear approximation, whereas the model predicted 23.1µstrain/cycle. These rates are relatively close. However, the tool material continued operating in phase C with a different accumulation rate before fracture, enduring more cycles than predicted by the model. Nevertheless, this final phase corresponds to an imminent failure condition and therefore represents a critical risk region for forging operation. Although the stress level in phases B and C was nearly the same, approximately 2,000MPa, the material response changed significantly before failure.

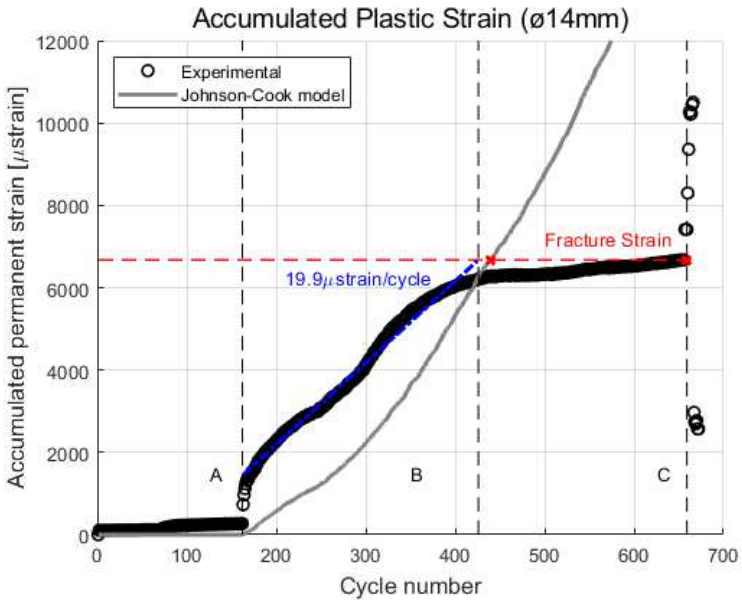


Fig. 9 Comparison of accumulated plastic strain in the H13 tool obtained from experimental data and the Johnson-Cook model

3.3 QForm FEM model

The finite element model developed in QForm provided the stress and strain values at each point of the tool, as illustrated in **Fig. 10** and **Fig. 11**, respectively. At the same location as the experimental strain-gauge, the plastic strain obtained from the FEM model was 17.34µstrain for one press cycle. The measured plastic strain for this cycle was 18.14µstrain, corresponding to a difference of 4.37% between the FEM model and the experimental data. In the FEM simulation, the effective stress distribution, shown in **Fig. 10**, was nearly uniform throughout the tool, with values close to 1,650MPa at the force peak. The maximum effective stress was 1,639.51MPa. However, the strain distribution showed relatively low and uniform plastic strain in the middle region of the tool, with concentrated values near the contact surface, as shown in **Fig. 11**. In this region, the maximum plastic strain reached 1,241.51µstrain. Therefore, the FEM model enabled the strain distribution along the tool geometry to be identified, while the local response was validated using the experimental measurement.

The time evolution of effective stress and effective strain is presented in **Fig. 12**, comparing the FEM model with the experimental strain measurements. In this case, the effective stress from the experimental data was calculated using Eq. (7). Both the stress and strain curves showed similar trends to the experimental measurements. However, the experimental data exhibited the influence of material hysteresis, which delayed the response and was not observed in the simulation. The maximum effective strains were 5,583.83µstrain and 6,528.91µstrain for the experimental data and simulation, respectively, corresponding to a difference of 16.93%. This difference is related to the adopted material properties and, mainly, to the hysteresis observed in the experimental curve. The maximum effective stresses were 1,667.98MPa and 1,599.43MPa for the experimental data and simulation, respectively, corresponding to a difference of 4.11%.

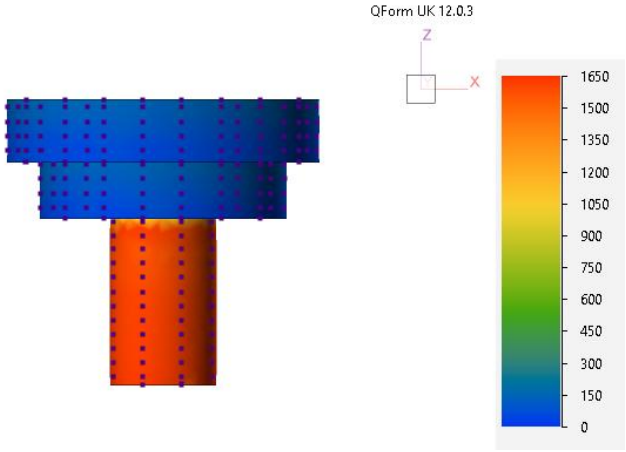


Fig. 10 Effective stress (MPa) predicted by the QForm FEM model at the maximum press force

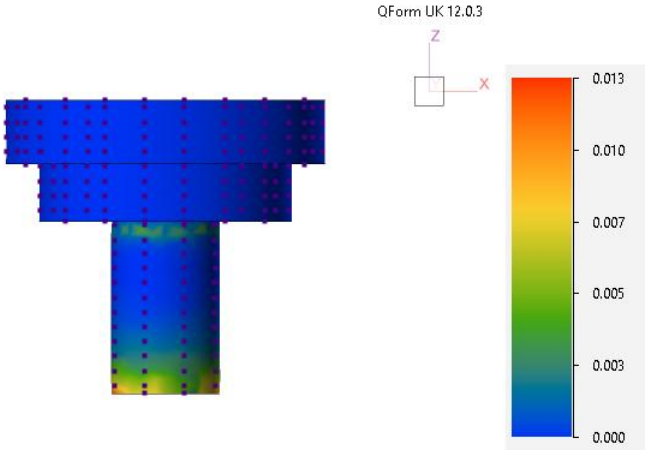


Fig. 11 Effective permanent strain (-) predicted by the QForm FEM model at the end of the press cycle

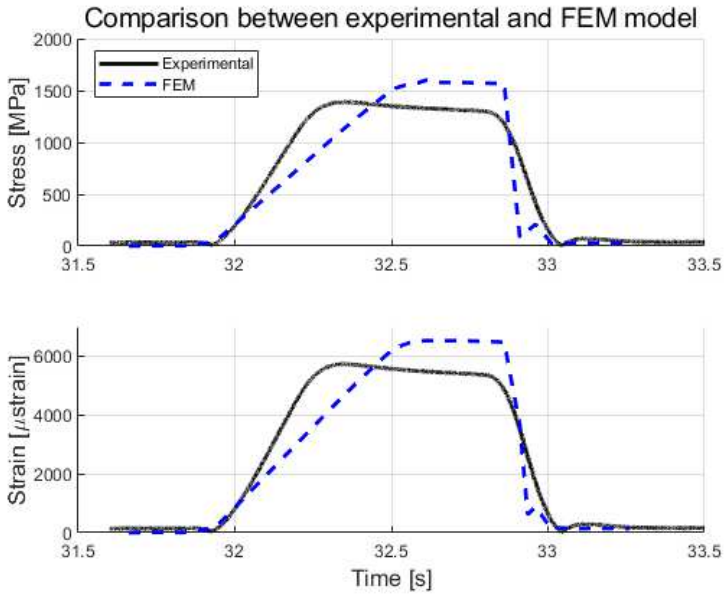


Fig. 12 Effective stress and effective strain: comparison between the QForm FEM model and experimental data

To generalize the methodology, the strain measurement location does not need to coincide with the maximum strain location. Instead, the strain-gauge can be installed at a practical position

where the measurement can be performed without interrupting machine operation. After updating the FEM model, the maximum strain obtained from the virtual model was used to estimate the maximum accumulated strain before failure. The maximum plastic strain for each cycle, ϵ_{max_i}, was calculated using a proportional relationship between the maximum plastic strain from the simulation, ϵ_{max}, and the strain at the measurement point, $\epsilon_{meas.point}$, as follows:

$$\epsilon_{max_i} = \frac{\epsilon_{max}}{\epsilon_{meas.point}} . \epsilon_{measured_i} \quad (20)$$

where $\epsilon_{measured_i}$ is the strain value measured by the strain-gauge in cycle i. Then, the accumulated strain at the maximum strain location was obtained as:

$$\epsilon_{total} = \sum \epsilon_{max_i} \quad (21)$$

The ratio between the maximum strain predicted by the FEM model and the experimentally measured strain was 68.45. Using this proportional factor, the cumulative plastic strain limit at the tool edge was estimated to be 0.46 strain. The estimated cumulative plastic strain limit is consistent with mechanical properties reported for H13 tool steel in the literature. Lei et al. (2022) obtained a yield strength of 1,468 MPa, an ultimate tensile strength of 1,837 MPa, and a fracture strain of 8.48% for H13 tool steel under uniaxial tensile loading. Yan et al. (2020) reported that tempered H13 steel reached a yield strength of 1,483 MPa, an ultimate tensile strength of 1,938 MPa, and a ductility of 5.8% after tempering at 600 °C. When the tempering temperature was increased to 700 °C, the ductility increased to 10.95%, although the strength decreased. Although these values were obtained from tensile tests, higher strain levels may be tolerated under the compressive stress state typical of forging operations. Furthermore, the strain magnitude estimated in the present work agrees with Marashi et al. (2017), who reported a strain of 0.38 for H13 steel during one working cycle under hot forging conditions.

3.4 Tool lifetime prediction

Based on the damage accumulation criterion, D, defined in Eq. (18), tool lifetime was predicted as the number of cycles for which the accumulated damage remained below 1. **Fig. 13** presents the expected damage accumulation from phase B onward, using the experimentally measured force history. In the Johnson-Cook model, the plastic strain is proportional to the stress estimated from the load-cell force. Therefore, the plastic strain increment varies according to the measured force in each cycle. In contrast, the FEM-based model assumes a constant plastic strain increment for each press cycle, since the simulation was adjusted for a specific cycle and does not account for the complete time-history response due to computational limitations. As shown in **Fig. 13**, the Johnson-Cook model reaches the damage limit ($D = 1$) near the beginning of phase C, at cycle 439, when material degradation approaches the tool strength limit. This result indicates that the analytical model identifies the transition from stable plastic strain accumulation to a critical damage condition before visible tool failure.

The prediction is conservative when compared with the experimentally observed fracture at cycle 656, but it is useful from a maintenance perspective because it anticipates the onset of a high-risk operating region. The rapid increase in damage predicted by this model would be consistent with the stress-dependent formulation, in which small variations in peak force near the material strength limit can produce significant changes in the estimated plastic strain increment. However, the linear increase predicted by the FEM-based model indicates a higher number of cycles to reach this limit, at cycle 547, within phase C. This represents an overestimation of tool lifetime, although the predicted failure still occurs before the experimentally observed fracture at cycle 656. This linear trend indicates that the model does not fully capture the nonlinear evolution of material degradation, principally, during the final stage of the test. As a result, the FEM-based model provides a better approximation of the critical region obtained from the spatial strain

distribution, but it has limited sensitivity to cycle-by-cycle variations in force and material degradation.

Overall, both models predicted failure before the experimentally observed fracture, indicating a conservative estimation of tool lifetime. The Johnson-Cook model was more sensitive to experimental force history and captured the acceleration of damage accumulation, whereas the FEM-based model provided information about the critical strain location and enabled the measured strain to be related to the maximum strain region of the tool. Therefore, the combination of both approaches provides a practical methodology for lifetime assessment. These results also show that, under low-cycle fatigue conditions, tool failure is governed not only by the maximum compressive stress but also by the progressive accumulation of permanent strain. High compressive loads did not immediately produce visible cracking; instead, damage accumulated during repeated press actuations until the material reached a critical degradation condition. Thus, monitoring permanent strain and using it as a damage indicator can support preventive maintenance decisions before visible tool failure occurs.

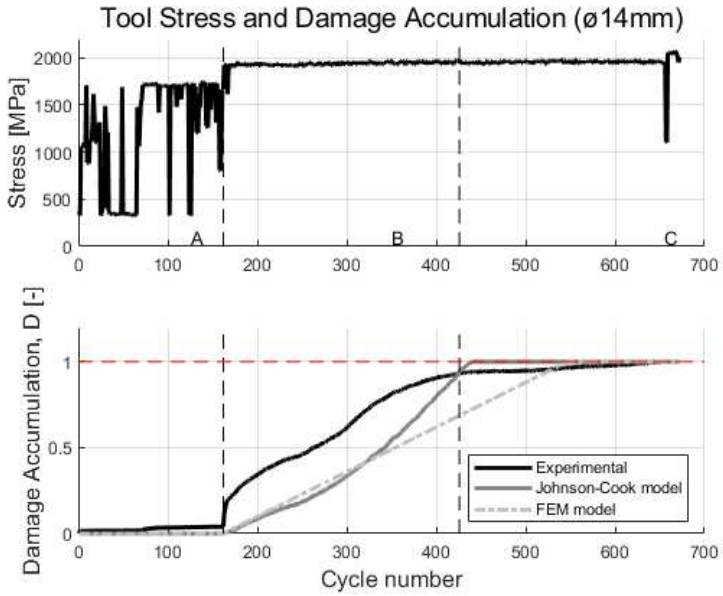


Fig. 13 Lifetime expectation from Johnson-Cook and FEM model

4. Conclusion

This study investigated the degradation of an AISI H13 cold forging tool caused by plastic strain accumulation under repeated hydraulic press actuations. The proposed methodology combined strain-gauge rosette measurements and load-cell force data with an analytical Johnson-Cook based plastic strain model and a QForm finite element model (FEM) to evaluate tool deformation and predict tool lifetime. Under the ambient-temperature and low strain-rate sensitivity conditions of the present test, the Johnson-Cook formulation reduced to a Ludwik-type hardening relation used to estimate the plastic strain increment from nominal stress. The experimental results showed that the tool response was initially dominated by elastic deformation at lower force levels, corresponding to phase A. However, after stabilization of the press force near 300kN, the permanent strain increased continuously, indicating progressive plastic deformation in phase B. Structural failure occurred at cycle 656, in phase C, when the accumulated permanent effective strain reached 6,674µstrain. At this stage, visible lateral bending and cracking near the support flange were observed. The adjusted Johnson-Cook model represented the plastic strain accumulation in the tool and predicted failure at cycle 439, corresponding to a lifetime approximately 33% lower than the experimental value, near the beginning of phase C. Although conservative, this prediction captured the transition to a critical damage condition between phases

B and C. The QForm FEM model reproduced the local plastic strain at the strain-gauge position with a difference of 4.37% and the maximum effective stress with a difference of 4.11% relative to the experimental data. The FEM-based lifetime prediction reached the damage limit at cycle 547, which was closer to the experimental fracture cycle in phase C, although still lower than the observed failure cycle. The results demonstrate that local strain measurements can be used to update analytical and numerical models for estimating plastic strain accumulation and tool lifetime. The methodology is useful when the strain-gauge cannot be installed at the maximum strain location, since the FEM model can be used to relate the measured strain to the critical region of the tool. Therefore, the integrated experimental and numerical approach provides a practical methodology for monitoring cold forging tool degradation and supporting maintenance decisions under fatigue conditions. Although the proposed methodology was validated using one instrumented tool failure test, additional tests under different force levels, tool geometries, and lubrication/ contact conditions are required to establish statistical confidence in the lifetime prediction.

5. Statements and Declarations

5.1 Funding

This study was financially supported by the Research Development Foundation (Fundação de Desenvolvimento da Pesquisa – Fundep), through the Rota 2030 Program, Line IV, grant number 27194*37.

5.2 Competing interests

The authors declare that they have no competing interests.

5.3 Data availability

The datasets generated and analyzed during the current study are available from the corresponding author upon request.

References

Ahmed IAA-K, Mohammed AI, Allow MA (2022) Improvement of forging die life by failure mechanism analysis. J Mech Behav Mater 30:309-317. https://doi.org/10.1515/jmbm-2021-0034

Behrens B-A, Brunotte K, Hübner S, Wester H, Müller F, Müller P, Wälder J, Matthias T (2021) Further development of wear calculation and wear reduction in cold forging processes. J Manuf Mater Process 5:36. https://doi.org/10.3390/jmmp5020036

Dabboussi W, Nemes JA (2005) Modeling of ductile fracture using the dynamic punch test. Int J Mech Sci 47:1282-1299. https://doi.org/10.1016/j.ijmecsci.2005.01.015

Dalbosco M, da Silva Lopes G, Schmitt PD, Pinotti L, Boing D (2021) Improving fatigue life of cold forging dies by finite element analysis: a case study. J Manuf Process 64:349-355. https://doi.org/10.1016/j.jmapro.2021.01.039

Ficak G, Łukaszek-Sołek A, Hawryluk M (2024) Durability of forging tools used in the hot closed die forging process: a review. Materials 17:5407. https://doi.org/10.3390/ma17225407

Gronostajski Z, Hawryluk M, Widomski P, Kaszuba M, Nowak B, Polak S, Rychlik M, Ziemba J, Zwierzchowski M (2019) Selected effective methods of increasing the durability of forging tools in hot forging processes. Procedia Manuf 27:124-129. https://doi.org/10.1016/j.promfg.2018.12.054

Hsia S-Y, Shih P-Y (2015) Wear improvement of tools in the cold forging process for long hex flange nuts. Materials 8:6640-6657. https://doi.org/10.3390/ma8105328

Kim DH, Kim BM, Kang CG (2005) Estimation of die service life for a die cooling method in a hot forging process. Int J Adv Manuf Technol 27:33-39. https://doi.org/10.1007/s00170-004-2100-0

Lachowicz MM, Ziemba J, Janik M, Trusz A, Hawryluk M (2025) Analysis of the deterioration mechanisms of tools in the process of forging elements for the automotive industry from nickel-chromium steel in order to select a wear-limiting coating. Materials 18:13. https://doi.org/10.3390/ma18010013

Lee YS, Lee JH, Ishikawa T (2002) Analysis of the elastic characteristics at forging die for the cold forged dimensional accuracy. J Mater Process Technol 130-131:532-539. https://doi.org/10.1016/S0924-0136(02)00800-2

Lei F, Wen T, Yang F, Wang J, Fu J, Yang H, Wang J, Ruan J, Ji S (2022) Microstructures and mechanical properties of H13 tool steel fabricated by selective laser melting. Materials 15:2686. https://doi.org/10.3390/ma15072686

Li Y, Ma D, Chi H, Zhang S, Zhou J, Cai J (2025) Fracture mechanism of H13 steel during tensile testing based on in situ EBSD. Metals 15:182. https://doi.org/10.3390/met15020182

Lisiecki Ł, Lisiecka-Graca P, Karkalos NE (2025) Analysis of crack initiation in hot forging process with the support of the digital image correlation system. Appl Sci 15:408. https://doi.org/10.3390/app15010408

Marashi J, Yakushina E, Xirouchakis P, Zante R, Foster J (2017) An evaluation of H13 tool steel deformation in hot forging conditions. J Mater Process Technol 246:276-284. https://doi.org/10.1016/j.jmatprotec.2017.03.026

Pan Q, Li Y, Huang M, Zhao Z, Ma P, Ma J (2019) Estimation of dynamic behaviors of hydraulic forging press machine in slow-motion manufacturing process. Nonlinear Dyn 96:339–362.

Petkar PM, Kulkarni VN, Sidalingeshwar IG, Umarfarooq MA, Khan T, Junaedi H, Sebaey TA (2026) Experimental investigation of die performance in cold forging backward extrusion. J Manuf Mater Process 10:70. https://doi.org/10.3390/jmmp10020070

Pilc J, Derbas M, Janota M, Kosut M (2014) Studying the implementation of potentiometric methods for the detection of cracks in renovation of forging tools. Commun Sci Lett Univ Zilina 16:90-95. https://doi.org/10.26552/com.C.2014.3A.90-95

Rohrmoser A, Hagenah H, Merklein M (2021) Adapted tool design for the cold forging of gears from non-ferrous and light metals. Int J Adv Manuf Technol 113:1833-1848. https://doi.org/10.1007/s00170-020-06449-6

Seo YH (2022) Development of smart cold forging die life cycle management system based on real-time forging load monitoring. Sci Rep 12:13297. https://doi.org/10.1038/s41598-022-17564-7

Varničić I, Pjević M, Popović M (2023) State of the art in the field of cold forging tools. In: Proceedings of XI International Conference Heavy Machinery HM 2023, Vrnjačka Banja, Serbia, 21-24 June 2023, pp C.13-C.18

Vianello PI, dos Santos AJ, Abrão AM, Magalhães FC (2020) Thermal fatigue analysis of hot forging closed dies. Mater Res 23:e20190697. https://doi.org/10.1590/1980-5373-MR-2019-0697

Wuertemberger L, Palazotto AN (2016) Evaluation of flow and failure properties of treated 4130 steel. J Dyn Behav Mater 2:207-222. https://doi.org/10.1007/s40870-016-0059-1

Yan J, Song H, Dong Y, Quach W-M, Yan M (2020) High strength (~2000 MPa) or highly ductile (~11%) additively manufactured H13 by tempering at different conditions. Mater Sci Eng A 773:138845. https://doi.org/10.1016/j.msea.2019.138845

Zhu X-K (2023) Effects of large plastic deformation and residual stress on the path independence of J-integral for cracks in ductile materials. Eng Fract Mech 277:108945. https://doi.org/10.1016/j.engfracmech.2022.108945